Synthetic empirical chorus wave model from combined Van Allen Probes and Cluster statistics

O.V. Agapitov, D. Mourenas, A.V. Artemyev, F. S. Mozer, G. Hospodarsky, J. Bonnell, Volodya Krasnoselskikh

Correspondence to:
O. V. Agapitov,
oleksiy.agapitov@gmail.com

Synthetic Empirical Chorus Wave Model From Combined Van Allen Probes and Cluster Statistics

O. V. Agapitov[1,2] (iD), D. Mourenas[3] (iD), A. V. Artemyev[4] (iD), F. S. Mozer[1] (iD), G. Hospodarsky[5] (iD), J. Bonnell[1], and V. Krasnoselskikh[6] (iD)

[1]Space Science Laboratory, University of California, Berkeley, CA, USA, [2]National Taras Shevchenko University of Kiev, Kiev, Ukraine, [3]CEA, DAM, DIF, Arpajon, France, [4]Institute of Geophysics and Planetary Physics, University of California, Los Angeles, CA, USA, [5]Department of Physics and Astronomy, University of Iowa, Iowa City, IA, USA, [6]LPC2E/CNRS, University of Orleans, Orleans, France

Abstract Chorus waves are among the most important natural electromagnetic emissions in the magnetosphere as regards to their potential effects on electron dynamics. They can efficiently accelerate or precipitate electrons trapped in the outer radiation belt, producing either fast increases of relativistic particle fluxes or auroras at high latitudes. Accurately modeling their effects, however, requires detailed models of their wave power and obliquity distribution as a function of geomagnetic activity in a particularly wide spatial domain, rarely available based solely on the statistics obtained from only one satellite mission. Here we seize the opportunity of synthesizing data from the Van Allen Probes and Cluster spacecraft to provide a new comprehensive chorus wave model in the outer radiation belt. The respective spatial coverages of these two missions are shown to be especially complementary and further allow a good cross calibration in the overlap domain. We used 4 years (2012–2016) of Van Allen Probes VLF data in the chorus frequency range up to 12 kHz at latitudes lower than 20°, combined with 10 years of Cluster VLF measurements up to 4 kHz in order to provide a full coverage of geomagnetic latitudes up to 45° in the chorus frequency range $0.1f_{ce} - 0.8f_{ce}$. The resulting synthetic statistical model of chorus wave amplitude, obliquity, and frequency is presented in the form of analytical functions of latitude and Kp in three different magnetic local time sectors and for two ranges of L shells outside the plasmasphere. Such a synthetic and reliable chorus model is crucially important for accurately modeling global acceleration and loss of electrons over the long run in the outer radiation belt, allowing a comprehensive description of electron flux variations over a very wide energy range.

1. Introduction

Whistler-mode chorus waves are among the most intense electromagnetic emissions recorded in the inner magnetosphere. They often occur in short, relatively coherent and repetitive bursts (e.g., Santolik et al., 2004) with rising or falling tones, which gave them their name. They cover a frequency range $0.1 - 0.8f_{ce}$ (with f_{ce} the equatorial electron gyrofrequency) and usually occur in two separate lower and upper frequency bands (LB and UB chorus, respectively, in the following text) with a power gap at $0.5f_{ce}$ (Sazhin & Hayakawa, 1992; Tsurutani & Smith, 1974). Chorus waves are generally observed above the plasmaspause from 23 MLT (magnetic local time) to 15 MLT, predominantly in the lower band, and with higher amplitudes during high geomagnetic activity (Agapitov et al., 2013; Burtis & Helliwell, 1976; Li et al., 2011; Meredith et al., 2001). UB waves interact resonantly mostly with lower-energy electrons (<50 keV) (e.g., Ma et al., 2016; Ni et al., 2011) while parallel and oblique LB chorus waves can affect all electrons from 0.1 keV to multi-MeVs (e.g., Artemyev et al., 2015), leading either to their stochastic local acceleration or their precipitation loss into the atmosphere—thereby being strongly involved in the quickly evolving dynamics of radiation belt electron fluxes (Artemyev et al., 2016; Horne et al., 2005; Li et al., 2014; Ma et al., 2016; Mourenas et al., 2014; Mourenas, Artemyev, Agapitov, Krasnoselskikh, Li, 2015; Mourenas et al., 2016; Ni et al., 2013, 2011; Shprits & Ni, 2009; Shprits et al., 2008; Su et al., 2015; Thorne et al., 2013; Tu et al., 2014). Precise models of the spatiotemporal distribution of chorus waves in the inner magnetosphere are thus crucially important for accurately simulating and forecasting the outer radiation belt variations.

However, due to the huge extent of the inner magnetosphere and because of limitations in the spatial coverage and instrumentation of satellites, a given spacecraft mission is generally unable to provide comprehensive,

accurate statistics of chorus waves encompassing the entire parameter space. Recently, Cluster satellites and the Van Allen Probes had sufficient instrumentation (notably, three-component magnetic amplitude measurements) and a very good spatial-temporal coverage between $L = 4$ and 6.6. Here we shall make use of 10 years of continuous Cluster measurements of chorus-type whistler waves that covered $4 \leq L \leq 7$ and all magnetic latitudes $|\lambda| < 45°$. Although this already represents a very large data set, it is worth noting that the low-latitude ($\lambda < 15°$) coverage of Cluster was limited at lower L. In contrast, the Van Allen Probes have now provided more than 4 years of coverage at $L \sim 1.5 - 6.5$ but restricted to low magnetic latitudes $\lambda < 20°$. These two missions therefore turn out to be complementary as regards to the latitudinal coverage. Moreover, the presence of an overlap of their respective latitudinal coverages at $\lambda \sim 15° - 20°$ allows a convenient cross calibration between these two different wave measurements. While other parameterizations of chorus amplitudes have been derived previously (Agapitov et al., 2015; Meredith et al., 2012; Spasojevic & Shprits, 2013), the present model has the unique advantage of relying on statistics from the two recent satellite missions possessing the most comprehensive and complementary spatiotemporal coverages, along with full three-component magnetic wave amplitude measurements.
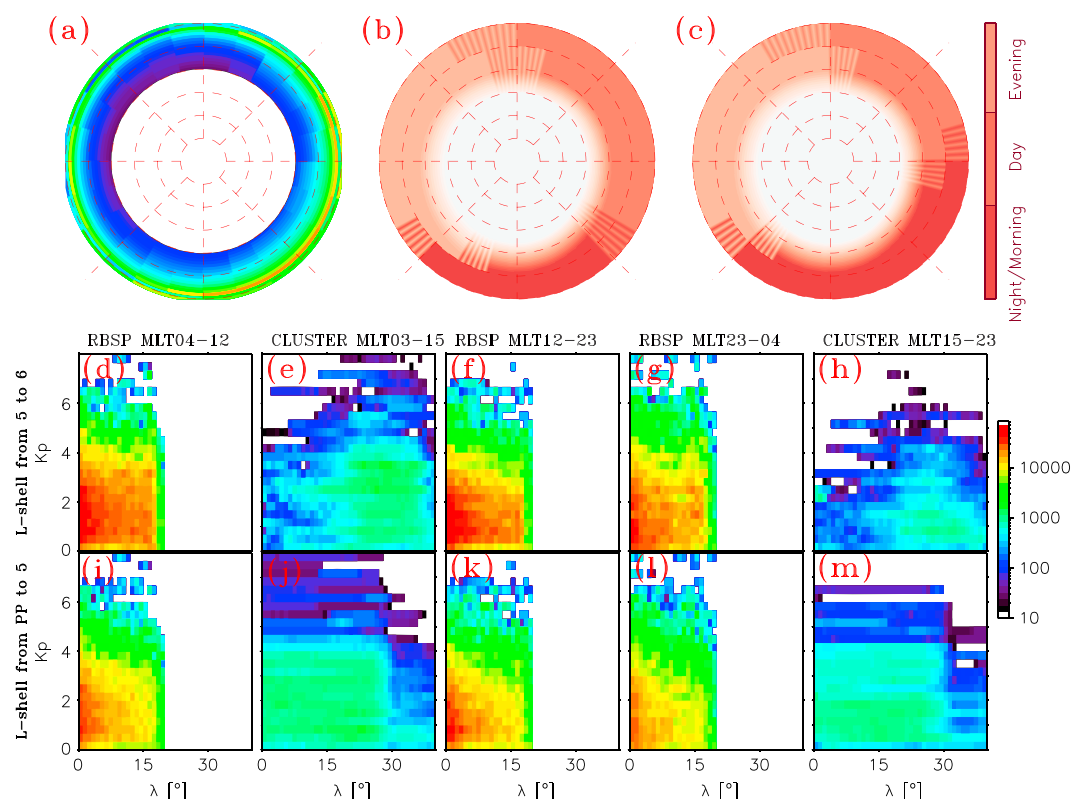
In the next section, we shall first provide an approximate model of the LB chorus frequency spectrum, making use of Cluster and Van Allen Probe statistics of the wave power distribution in frequency, known to depend on latitude (Breuillard et al., 2015; Bunch et al., 2013), before describing, in more detail, the differences and complementarity of the orbital coverage of these two missions. In particular, we shall demonstrate the necessity of supplementing the comprehensive Van Allen Probes statistics available at low latitudes by Cluster data at higher latitudes for accurately evaluating energization and loss of MeV and multi-MeV (so-called "killer") electrons that pose a high risk to satellite electronic equipment (e.g., Horne et al., 2013, and references therein). Then, we will provide detailed statistics and models of LB and UB chorus wave amplitudes in three separate MLT sectors and two L ranges, making use of Van Allen Probes and Cluster statistics. An instructive cross calibration will be performed in the range comprised between the plasmapause and $L = 5$ for $|\lambda| < 20°$ in the day sector, where both Cluster and the Van Allen Probes had significant coverage. We shall take precisely into account the frequency limitation (upper limit of 4 kHz) in Cluster measurements and its varying impact as latitude increases to renormalize Cluster lower-band chorus amplitudes to better correspond to the full (actual) spectra (see details in Agapitov et al., 2015). A synthetic empirical model of chorus wave root-mean-square (RMS) amplitudes, based on both the corresponding cross-calibrated Cluster statistics and Van Allen Probe measurements, will be provided over the whole parameter domain $L \sim 4 - 6$ above the plasmapause and for $|\lambda| < 45°$. The next section will use Van Allen Probe data to confirm and improve upon the chorus wave obliquity model previously provided and based on the sole Cluster statistics (Agapitov et al., 2015). The last section will compare energy and pitch angle diffusion rates calculated using the new synthetic chorus model with results obtained using previous chorus models, highlighting the importance of considering a comprehensive, realistic wave model.

2. Complementarity of Van Allen Probes and Cluster Orbital Coverages

2.1. Generalities

Quasi-linear pitch angle and energy diffusion of electrons by chorus waves can be calculated by Fokker-Planck codes (Horne et al., 2013; Su et al., 2015; Thorne et al., 2013; Tu et al., 2014) or estimated analytically (Albert, 2008, 2007; Artemyev et al., 2016; Mourenas et al., 2014; Mourenas, Artemyev, Agapitov, Krasnoselskikh, Li, 2015). In all cases, however, two important parameters are the magnetic latitude, where cyclotron resonance can occur between electrons and waves with a given mean frequency, and the corresponding amplitude of the waves at that latitude. If wave data are unavailable in this latitudinal range for a given electron energy, then it is obviously impossible to evaluate the effects of chorus waves on such electrons.

The Van Allen Probes (Mauk et al., 2012) are two identical NASA spacecraft launched on 30 August 2012, to provide, since that time, a wealth of particle and field measurements inside the Earth's radiation belts. These two probes are in nearly identical orbits (perigee of 600 km, apogee about 6 Earth radii, and period of 9 h) covering low latitudes. Electric and magnetic field waveforms are provided by the Electric Fields and Waves (EFW) (Wygant et al., 2013) and the Electric and Magnetic Field Instrument Suite and Integrated Science (EMFISIS) (Kletzing et al., 2013) payloads. Power spectra and full spectral matrices are transmitted continuously in 72 logarithmically spaced frequency channels. FluxGate magnetometer (part of the EMFISIS experiment) measurements were employed for evaluating the background magnetic field magnitude (Kletzing et al., 2013). To extend the coverage to higher latitudes, we use the large data set collected on board Cluster by the
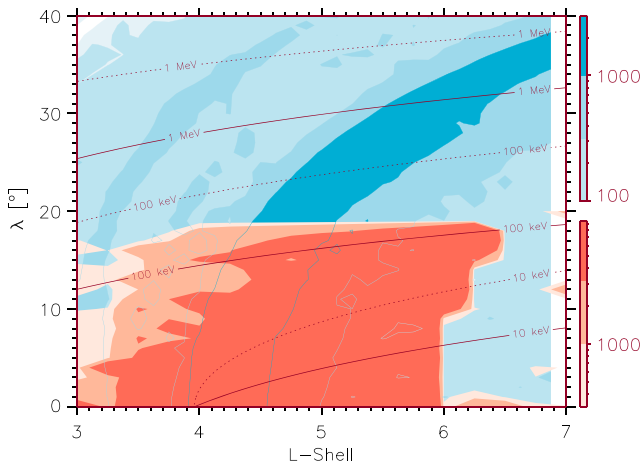
Figure 1. Data coverage of measurements at $L = 4–6$ from EMFISIS on board the Van Allen Probes in 2012–2016 (a) and from CLUSTER STAFF-SA during 2001–2010 in the chorus frequency range ($0.1f_{ce} < f < f_{ce}$), given as the number of spectra captured in a magnetic latitude λ-Kp domain for day/night sector and two L shell ranges: (d–m) from 4 to 5 and from 5 to 6. The wave amplitude model sectors are indicated by color for (b) lower band and (c) upper band chorus.

Spatio-Temporal Analysis of Field Fluctuations - Spectrum Analyzer (STAFF-SA) instrument (Cornilleau-Wehrlin et al., 2003) from 2001 to 2010, as presented in Agapitov et al. (2013, 2015). The frequency bands of Van Allen Probes EMFISIS and Cluster STAFF-SA are well sampled and, for both instruments, the integrated wave intensity can be calculated, providing good measurements in the chorus frequency range. The upper limit of STAFF-SA is 4 kHz, so that measurements in the UB chorus frequency range are only available for $L > 6$. Thus, the analysis of the UB frequency range throughout this paper is based solely on Van Allen Probes EMFISIS measurements. This 4 kHz limit of Cluster also restricts the coverage of the LB chorus frequency range when $L < 4.5$, and an appropriate correction to the full spectrum intensity has been applied at latitudes below 15–20° (see details in Agapitov et al., 2015).

The VLF wave observation coverage of the Van Allen Probes at $L=4–6$ is shown in Figure 1a. Van Allen Probes measurements were carried out over $L = 2–6$ at geomagnetic latitudes below 15–20° with a full MLT cycle taking 2 years. For a given geomagnetic activity level, the wave power distribution can be approximately modeled in three separate MLT domains where the distribution remains roughly similar when performing Kolmogorov-Smirnov comparisons (see details in Agapitov et al., 2015): dayside (or dawnside/dayside—from 6:00 to 14:00 MLT), evening sector (from 14 to 22 MLT), and nightside (from 22 to 6 MLT). In addition, each MLT domain can be split into two L regions: $L \in [4, 5]$ and $L \in [5, 6]$ (Agapitov et al., 2013). In the corresponding six subregions color coded in Figure 1b for LB chorus and in Figure 1c for UB chorus, wave power depends on latitude λ and geomagnetic activity level (Kp index here). The Van Allen Probes and Cluster coverages of these six subregions as a function of Kp are indicated in Figures 1d–1m. The wave power latitudinal dependence has been approximated in the past in widely different ways: step functions (Ni et al., 2011; Thorne et al., 2013), polynomials limited to $|\lambda| < 15°$ (Spasojevic & Shprits, 2013), or polynomials over a wide λ domain based on the sole Cluster data (Agapitov et al., 2015).

However, determining the full latitudinal distribution of wave intensity is critically important for accurately modeling electron acceleration and loss as a function of particle energy because each electron energy range
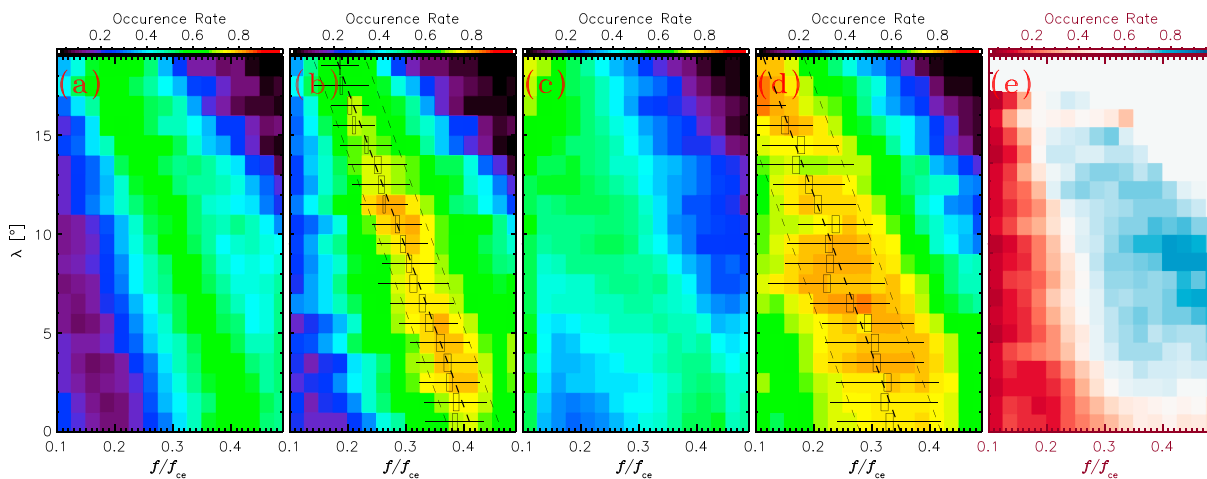
Figure 2. Locations of cyclotron resonance for electrons with low equatorial pitch angles (near their loss cone) interacting with LB chorus waves with field-aligned wave normal angles in the L Shell/λ domain, estimated using the synthetic wave power frequency distribution obtained from Cluster and the Van Allen Probes and discussed in section 2.2 (solid black curves). The approximations based on simply considering a fixed $f = 0.35 f_{ce}$ are shown by dashed curves. Measurement coverages for Cluster and the Van Allen Probes are shown by blue and red contours, respectively.

corresponds to a particular, limited latitudinal range for cyclotron resonance with chorus waves (generally appropriate for estimating loss rates of electrons, see Shprits et al., 2006). Let us use the mean chorus frequency distribution model provided below in section 2.2 (based on Cluster and Van Allen Probes statistics) and the plasma trough density model from Sheeley et al. (2001). On this basis, Figure 2 shows that low equatorial pitch angle MeV and multi-MeV electrons reach cyclotron resonance with LB chorus waves only beyond the $\lambda = 20°$ upper limit of the coverage available from the Van Allen Probes (indicated by the red color) but fully within the coverage provided by Cluster (indicated by the blue color). On the other hand, electron energization mostly occurs at high equatorial pitch angles where cyclotron resonance with chorus waves is reached at low latitudes $\lambda < 10°-20°$ (e.g., Horne, Horne, et al., 2005; Mourenas et al., 2014) where Cluster coverage is more sparse. This demonstrates the nice complementarity of the orbital coverages of Cluster and the Van Allen Probes, as well as the usefulness of building a synthetic chorus model by carefully combining wave statistics from these two missions, to allow a complete description of both chorus-induced electron acceleration and loss.
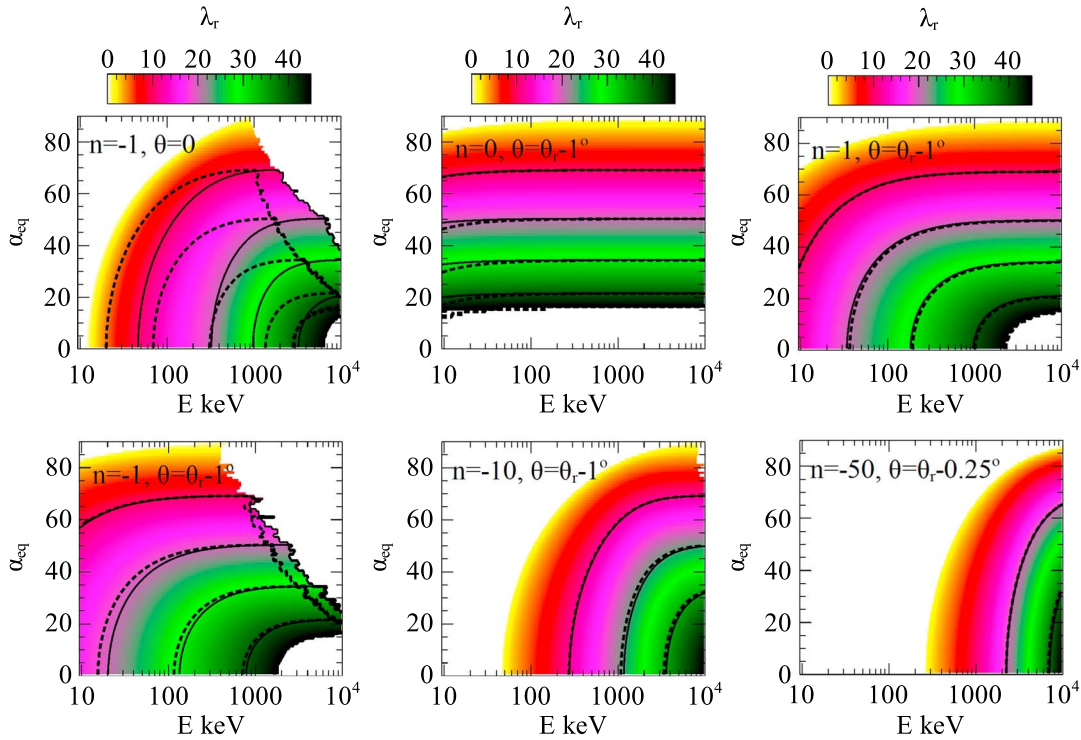
2.2. Chorus Wave Power Distribution in Frequency

Quasi-linear diffusion rates depend almost linearly on the value of the mean chorus wave frequency (Mourenas et al., 2014; Mourenas, Artemyev, Agapitov, Krasnoselskikh, Li, 2015). To be complete and reliable for the computation of electron scattering, a synthetic chorus model must therefore include a model of the wave frequency distribution. Figure 3 sh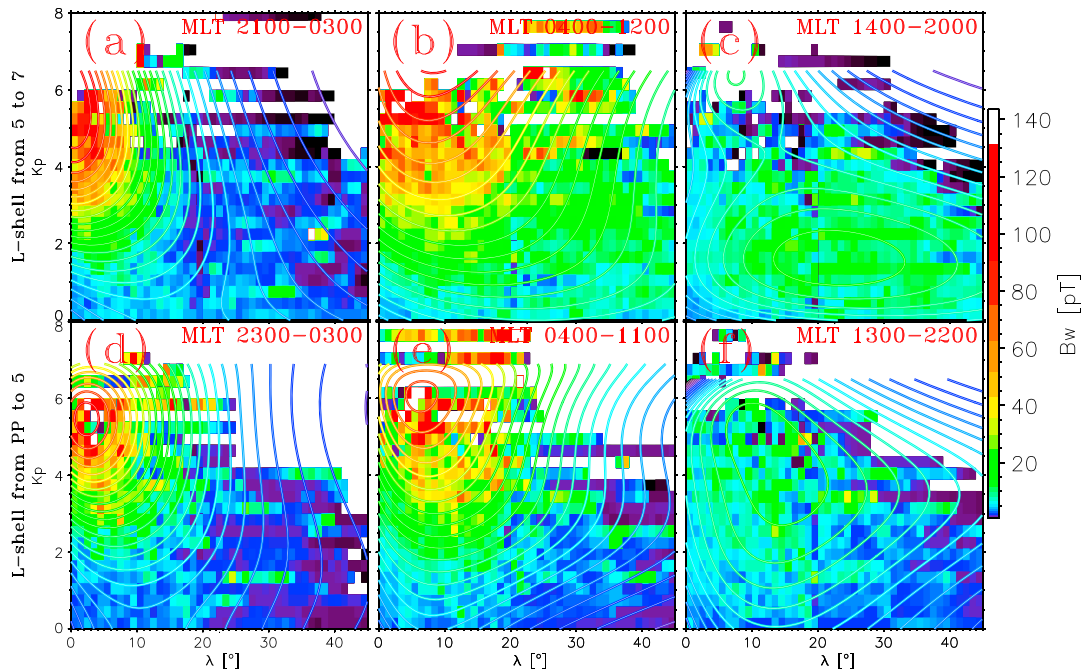ows this frequency distribution of LB chorus waves as a function of magnetic latitude, obtained by combining Cluster and Van Allen Probe statistics. Based on previous studies (Agapitov et al., 2013; Agapitov et al., 2016; Artemyev et al., 2016; Li et al., 2013; Li, Santolik, et al., 2016; Mourenas et al., 2014; Taubenschuss et al., 2014), we considered separately two groups of waves: quasi-parallel and very oblique waves (near the resonance cone). Figure 3a shows the occurrence distribution of very oblique LB chorus wave frequency, while Figure 3b displays the same occurrence distribution weighted by wave power. The wave power distribution is roughly Gaussian at each λ and the mean wave frequency f_m continuously decreases with increasing of latitude from $0.4 \pm 0.02 f_{ce}$ at the equator down to $f_m = 0.2 f_{ce}$ at $\lambda = 20°$, demonstrating an approximately constant variance σ_f (shown by horizontal error bars). The dependence of f_m on λ is well reproduced by the linear fit $f_m/f_{ce} = 0.41 - 0.0125 * \lambda$ indicated in Figure 3b by a solid dashed line (thin lines showing the variance equal to 0.05). Similar plots for quasi-parallel

Figure 3. Lower-band chorus wave maximum (probability distribution function) PDF and PDF weighted by wave intensity B_w^2 as a function of λ for (a, b) oblique and (c, d) parallel waves. The maximum (squares) and variance (error bars) are indicated in Figures 3b and 3c. The model mean frequency is shown by a thick dashed line and the variance by thin dashed lines. Figure 3e presents the respective occurrence rates of oblique (blue) and parallel (red) chorus waves $N_{ow}/(N_{ow} + N_{pw})$ in the $f/f_{ce} - \lambda$ domain.

Figure 4. Localization of resonances with LB chorus waves in the energy/pitch angle domain estimated using the synthetic wave power frequency distributions obtained from Cluster and the Van Allen Probes. $\lambda = 10, 20, 30°$ are indicated by black solid curves. Localizations of resonances corresponding to $\lambda = 10, 20, 30°$ based on the simplified model of constant $f_m = 0.35 f_{ce}$ are also shown by dashed lines. Parallel waves (top left panel) and very oblique waves close to the resonance cone angle θ_r are considered for cyclotron or Landau ($n=0$) resonances.

Figure 5. Van Allen Probes ($\lambda < 20°$)and Cluster ($\lambda > 20°$) measurements of LB chorus RMS amplitudes are shown by solid colors for three MLT (indicated in the panels) sectors and two L shell ranges as in Figure 1. The synthetic model of LB chorus RMS amplitude B_w provided as a continuous function of Kp and λ is shown by contours of corresponding colors in the day, evening, and night sectors of the magnetosphere for $L \sim 4-5$ and $L = 5-6$ above the plasmapause.

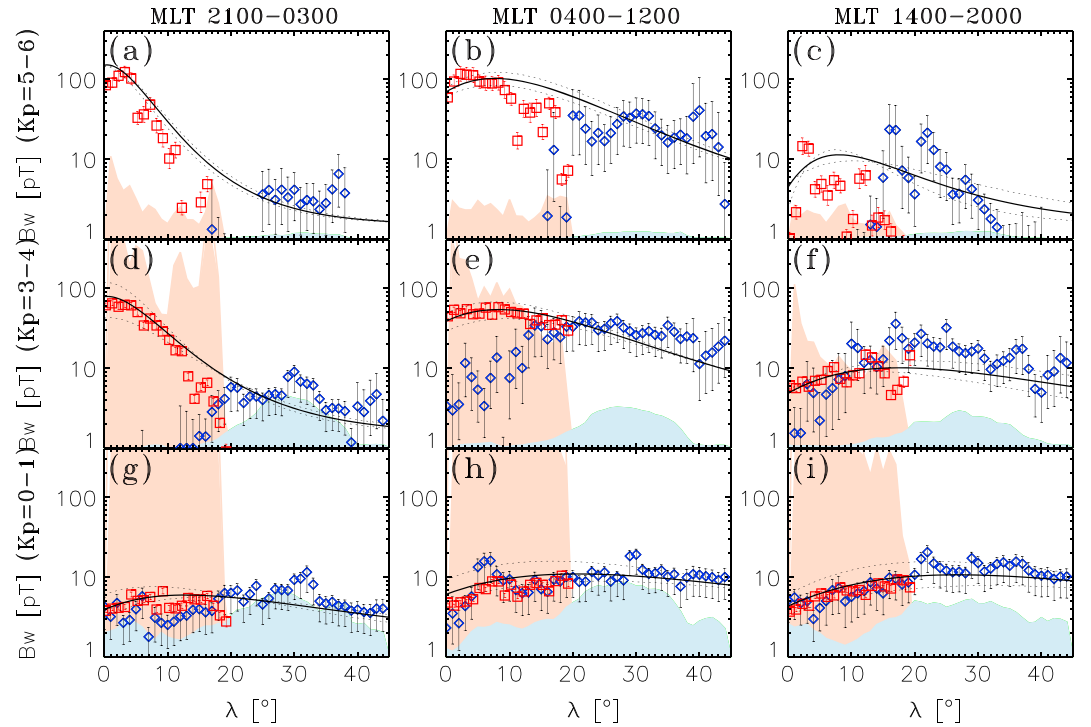**Figure 6.** Lower-band chorus wave RMS amplitudes B_w as a function of λ in the day, evening, and night sectors of the magnetosphere for $L \sim 4 - 5$ above the plasmapause and in different Kp ranges. Cluster and Van Allen Probes measurements are shown by blue and red points, respectively, and the corresponding number of available samples are indicated by light blue and light red (the Van Allen Probes number of samples being multiplied by a factor of 5 for better visibility). The synthetic model of lower-band chorus RMS amplitudes is shown by a black curve in each parameter domain.

waves fit $f_m/f_{ce} = 0.35 - 0.0125 * \lambda$ with a variance of 0.07 are presented in Figures 3c and 3d. Quasi-parallel waves have a similar, close to linear, dependence on λ with smaller mean frequencies (with larger variance σ_f) than very oblique waves. Low-frequency waves are mainly parallel whereas high-frequency waves are mainly very oblique (see relative occurrence rate in Figure 3e).

This new synthetic wave frequency model, obtained by combining data from the Van Allen Probes and Cluster in different latitude ranges, roughly agrees with previous results from ray tracing simulations, Cluster statistics alone (Agapitov et al., 2013; Breuillard et al., 2012, 2015; Chen et al., 2013), Polar data (Bunch et al., 2013), and other work demonstrating the generally separate occurrences in time and in the MLT domain of very oblique and parallel lower-band chorus waves (Agapitov et al., 2016; Li, Santolik, et al., 2016). A mean lower-band chorus frequency $f_m = 0.35f_{ce}$ has often been used in past studies (e.g., Artemyev et al., 2013; Horne, Horne, et al., 2005; Shprits et al., 2006). Significant variations of the positions of cyclotron resonances are seen in Figure 4 when using the actual mean frequency (solid black curves) determined from Van Allen Probes and Cluster data, versus using $f_m = 0.35f_{ce}$ (dashed black curves). Such differences arise when the actual f_m becomes smaller than $0.35f_{ce}$, because the cyclotron resonant electron momentum squared at fixed latitude varies roughly as the inverse of the wave frequency for low electron pitch angles and energies <1 MeV (e.g, Mourenas, Artemyev, Agapitov, Krasnoselskikh, Li, 2015). The corresponding electron diffusion rates will be processed in section 5.

3. Synthetic Lower-Band and Upper-Band Chorus Amplitude Model

The most intense LB and UB chorus waves are observed mainly in the sector from 23 to 14 MLT, corresponding to the eastward drift of energetic electrons injected into the inner magnetosphere around midnight (Li et al., 2010). The wave RMS amplitude B_w depends on L shell, with a maximum in the core of the outer radiation belt (Agapitov et al., 2013; Meredith et al., 2001, 2012). The latitudinal distribution of the RMS amplitude that is presented in Figure 5 depends on MLT and on the level of geomagnetic activity. Cluster statistics show that the amplitude maximum is shifted away from the geomagnetic equator (Agapitov et al., 2013, 2015;

Figure 7. Lower-band chorus wave RMS amplitudes B_w as a function of λ in the day, evening, and night sectors of the magnetosphere for $L \sim 5 - 6$ above the plasmapause and in different Kp ranges. Cluster and Van Allen Probes measurements are shown by blue and red points, respectively, and the corresponding number of available samples are indicated by light blue and light red (the Van Allen Probes number of samples being multiplied by a factor of 5 for better visibility). The synthetic model of lower-band chorus RMS amplitudes is shown by a black curve in each parameter domain.

Meredith et al., 2012) where chorus waves are generated (e.g., Agapitov et al., 2013; Artemyev et al., 2016; LeDocq et al., 1998; Li et al., 2013; Mourenas, Artemyev, Agapitov, Krasnoselskikh, Mozer, 2015), suggesting a continuous amplification of the waves during their propagation up to ∼15°. A correct estimation of wave amplitudes around the latitude of resonance requires providing a model of the amplitude distribution as a function of λ and geomagnetic activity, as was provided earlier, based on Cluster data alone (Agapitov et al., 2015). Using additional Van Allen Probe measurements allows understanding what happens in the low-latitude region insufficiently covered by the Cluster satellites (see Figure 1): most notably, the presence of very high intensity LB waves in the night sector near the magnetic equator (Figures 5a and 5d).

A cross calibration between Cluster and Van Allen Probe RMS B_w levels has been performed in the day sector over the latitudinal range $|\lambda| < 20°$ where the coverage is good for both missions (Figures 1i and 1j). The different regimes of wave intensity evaluation (Cluster STAFF-SA provides wave properties averaged over a 4 s interval whereas the Van Allen Probe EMFISIS instrument provides data obtained for a 0.5 s averaging) lead to a 3 times larger variance of the distribution for Van Allen Probes. Nevertheless, RMS values agree within a factor of 1.5 in general in this region — that is, the discrepancy remains less than the sum of the respective uncertainties (see Figures 6 and 7). This indicates that Cluster data can indeed be used to supplement Van Allen Probes data that are only available at low latitudes.

To closely reproduce the observed distributions, the chorus wave amplitude model has been developed with the following form:

$$\lg B_w(\lambda, Kp)[\text{nT}] = b_0 \cdot (\lambda - b_3) \cdot \exp(-\lambda \cdot b_2 - b_1) \tag{1}$$

where $b_i = \sum a_{ij} Kp^j$ and coefficients a_{ij} (listed in Table 1) have been evaluated to provide good global fits to Van Allen Probe and Cluster measurements. Note that the synthetic analytic fitting formulas provide a smooth, continuous modeling as a function of parameters (Kp, λ). It allows reasonable estimates, even in
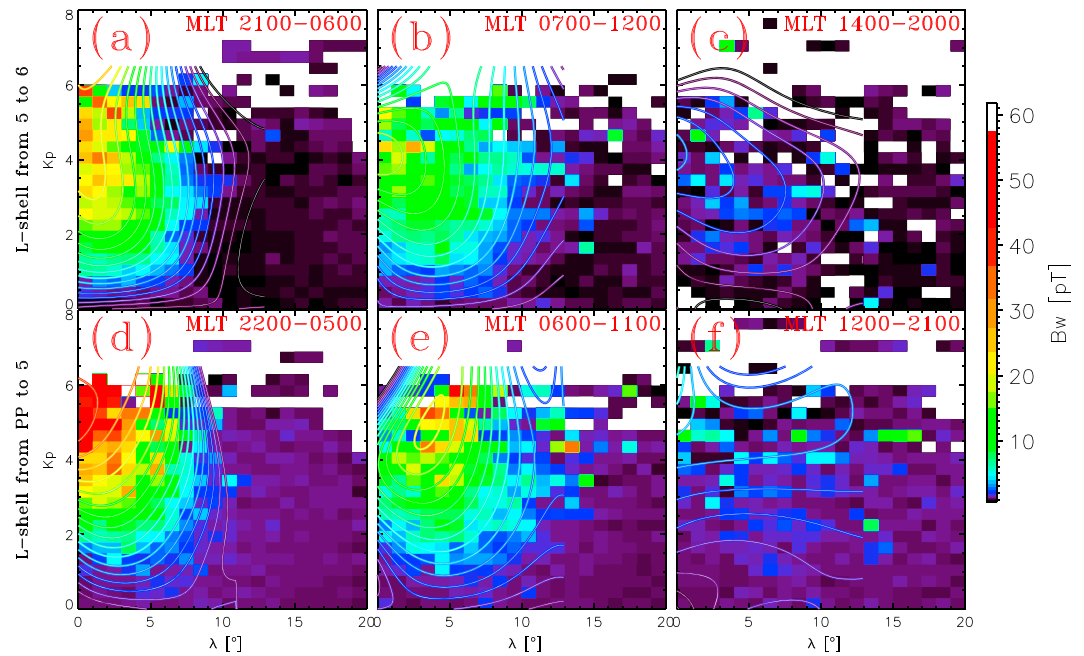
Table 1
Coefficients α_{ij} for the Model of LB Chorus RMS Amplitude B_w

Sector	ij	0	1	2	3
			Night/Morning (MLT 23–04)		
$PP < L < 5$	1	$4.1877 \cdot 10^{-1}$	$-9.0608 \cdot 10^{-3}$	$5.2279 \cdot 10^{-2}$	$-6.5120 \cdot 10^{-3}$
	1	1.5863	$1.4375 \cdot 10^{-1}$	$-9.3020 \cdot 10^{-2}$	$9.3822 \cdot 10^{-3}$
	1	$7.4082 \cdot 10^{-2}$	$-6.8803 \cdot 10^{-3}$	$6.3612 \cdot 10^{-3}$	$-6.8278 \cdot 10^{-4}$
	1	-2.4300	-2.1121	$3.6348 \cdot 10^{-1}$	$-2.0494 \cdot 10^{-2}$
$5 < L < 6$	1	$3.2203 \cdot 10^{-1}$	$8.2359 \cdot 10^{-3}$	$4.6659 \cdot 10^{-2}$	$-5.4544 \cdot 10^{-3}$
	2	1.7732	$6.0086 \cdot 10^{-2}$	$-8.5062 \cdot 10^{-2}$	$9.6633 \cdot 10^{-3}$
	3	$4.5626 \cdot 10^{-2}$	$9.2193 \cdot 10^{-3}$	$3.4485 \cdot 10^{-3}$	$-4.2794 \cdot 10^{-4}$
	4	-5.7878	-5.2970	1.7597	$-1.5317 \cdot 10^{-1}$
			Day (MLT 04–12)		
$PP < L < 5$	1	$5.5884 \cdot 10^{-1}$	$-1.3011 \cdot 10^{-1}$	$7.9472e\text{-}002$	$-9.2103 \cdot 10^{-3}$
	2	1.4989	$4.5649 \cdot 10^{-2}$	$-2.1041 \cdot 10^{-2}$	$3.7914 \cdot 10^{-4}$
	3	$9.9792 \cdot 10^{-2}$	$-3.3988 \cdot 10^{-2}$	$1.0392 \cdot 10^{-2}$	$-9.0381 \cdot 10^{-4}$
	4	-1.9441	-3.3455	$8.5083 \cdot 10^{-1}$	$-7.2328 \cdot 10^{-2}$
$5 < L < 6$	1	$2.4510 \cdot 10^{-1}$	$9.6416 \cdot 10^{-2}$	$-8.3788 \cdot 10^{-3}$	$3.5775 \cdot 10^{-4}$
	3	1.7767	$-6.0993 \cdot 10^{-2}$	$2.4017 \cdot 10^{-3}$	$-5.5076 \cdot 10^{-5}$
	4	$2.7606 \cdot 10^{-2}$	$5.9185 \cdot 10^{-3}$	$-1.3959 \cdot 10^{-4}$	$-4.0953 \cdot 10^{-5}$
	5	$-1.2235 \cdot 10$	-1.2452	$2.8956 \cdot 10^{-1}$	$-1.4832 \cdot 10^{-2}$
			Evening (MLT 12–23)		
$PP < L < 5$	1	$4.8179 \cdot 10^{-1}$	$2.2206 \cdot 10^{-2}$	$-2.1949 \cdot 10^{-2}$	$4.0690 \cdot 10^{-3}$
	2	1.5997	$-9.9165 \cdot 10^{-2}$	$7.1753 \cdot 10^{-2}$	$-1.0798 \cdot 10^{-2}$
	3	$6.1269 \cdot 10^{-2}$	$-1.2257 \cdot 10^{-3}$	$-3.7738 \cdot 10^{-3}$	$7.7571 \cdot 10^{-4}$
	4	-2.7227	-1.2788	$-4.9845 \cdot 10^{-1}$	$1.2404 \cdot 10^{-1}$
$5 < L < 6$	1	$2.1277 \cdot 10^{-1}$	$2.0086 \cdot 10^{-1}$	$-8.4907 \cdot 10^{-2}$	$1.1070 \cdot 10^{-2}$
	2	$1.7252e$	$-9.2292 \cdot 10^{-2}$	$5.7363 \cdot 10^{-2}$	$-9.2312 \cdot 10^{-3}$
	3	$2.4257 \cdot 10^{-2}$	$1.0763 \cdot 10^{-2}$	$-5.4592 \cdot 10^{-3}$	$9.8882 \cdot 10^{-4}$
	4	$-9.2179e$	$-5.3855 \cdot 10^{-1}$	$1.7238 \cdot 10^{-1}$	$2.0337 \cdot 10^{-2}$

narrow parameter domains where the coverage by all these satellites is sparse, because of the weighted contribution from neighboring parameter domains to the global fitting. This is more apparent in Figure 5, where the synthetic model of lower-band chorus amplitude is displayed as a continuous function of both Kp and latitude. In particular, the two trends of amplitude decrease toward high latitudes and amplitude increase with Kp found in regions of excellent coverage have an (indirect) effect on neighboring parameter regions with less coverage, where these trends naturally continue. Cluster coverage is very sparse for $Kp > 6$–7 at latitudes $> 35°$, but the (measured and modeled) wave amplitudes are relatively low there, mitigating the potential consequences on global electron dynamics.

Figures 6 and 7 display the respective distributions of lower-band chorus RMS amplitudes B_w obtained from EMFISIS (red points) and from STAFF-SA (blue points) as a function of magnetic latitude for different Kp and L ranges. Note that a correction factor has been applied to Cluster RMS B_w values to make up for the limited frequency range of Cluster LB chorus measurements at low $L < 5$, as compared with the full lower-band chorus spectrum width known from other satellites (Polar and Van Allen Probes, see section 2.2). At $\lambda \geq 15°$ or for $L > 5$, the correction factor is about unity, but amplitude levels from Cluster for $L > 5$ at $\lambda < 15°$ become clearly unreliable due to the very sparse orbital coverage there (see Figure 1).

Although the LB chorus model from Agapitov et al. (2015) based solely on Cluster data already provided a fitting of wave amplitudes from low to high latitudes, it still suffered from insufficient coverage at low latitudes, especially on the nightside at $L \geq 5$ (see Figure 1) where most MeV electron energization often occurs (Horne et al., 2005; Mourenas et al., 2014; Thorne et al., 2013). Thus, the relatively good coverage of magnetic latitudes

Figure 8. Van Allen Probes ($\lambda < 20°$) and Cluster ($\lambda > 20°$) measurements of UB chorus RMS amplitudes are shown by solid colors for three MLT (indicated in the panels) sectors and two L shell ranges as in Figure 1. The synthetic model of UB chorus wave RMS amplitudes B_w as a continuous function of Kp and λ is shown by contours of corresponding color in the day, evening, and night sectors of the magnetosphere for $L \sim 4$–5 and $L = 5$–6 above the plasmapause.

$\lambda > 15°$ from Cluster can be complemented by the very good near-equatorial coverage from the Van Allen Probes to obtain a comprehensive chorus model extending from the equator to 45° over $Kp \sim 0$–6 and $L \sim 4$–6 (see Figures 1–3).

Note that Van Allen Probe data samples were obtained with a resolution of 0.5 s whereas Cluster resolution was 4 s. This leads to a larger number of samples from the Van Allen Probes and larger instantaneous wave power values. However, time averaging the 0.5 s samples from the Van Allen Probes over long timescales as in Figures 6 and 7 should lead to similar intensity levels as obtained from Cluster data in the same (spatial and Kp) parameter range, provided that both instruments were similarly well calibrated. Because the Van Allen Probe period 2012–2016 was characterized by a lower average geomagnetic activity than the Cluster 2001–2010 period, however, it is especially important to separate wave intensity levels in relatively narrow Kp ranges.

Some interesting general features can be emphasized in Figures 5–7 as regards the distribution of RMS lower-band chorus amplitudes B_w as a function of latitude, MLT, and Kp. The amplitude distribution has a peak near the equator in the night sector, decreasing toward higher latitudes more quickly as Kp increases. The distribution peak moreover shifts toward higher latitudes as one goes from the nightside to the day sector and, then, to the evening sector, sometimes reaching ~25°. Finally, wave amplitudes at $\lambda < 20°$ are smallest in the evening sector. All these features probably stem from variations of the low-energy (0.1–30 keV) electron population distribution responsible for chorus wave growth and damping. In particular, the strongly anisotropic electron population injected in the midnight sector progressively loses its anisotropy as it drifts toward later MLT regions, while the lower-energy population (<1–3 keV) gets precipitated into the atmosphere and produces less damping. The fine balance between these various processes likely produces the different wave intensity distributions observed in different local time sectors.

UB chorus waves have weaker amplitudes than LB waves and are moreover confined to a region within <10° from the magnetic equator (see also Meredith et al., 2012, 2009). This makes Van Allen Probe measurements particularly well adapted for a comprehensive analysis of UB chorus properties. Their peak intensities reach the order of a few hundred pT during active conditions between 23 and 11 MLT from $L = 3$ (during high geomagnetic activity) to $L = 7$. The corresponding wave power is concentrated at $f \sim 0.5$–$0.6 f_{ce}$ with rather constant $f_m \sim 0.55 f_{ce}$ and variance $\sim 0.05 f_{ce}$. A statistical analysis of the wave amplitude distribution in various MLT sectors and L shell bins leads to a convenient splitting into six regions, as shown in Figure 1c. The distribution

Table 2
Coefficients α_{ij} for the Model of UB Chorus Wave RMS Amplitude B_w

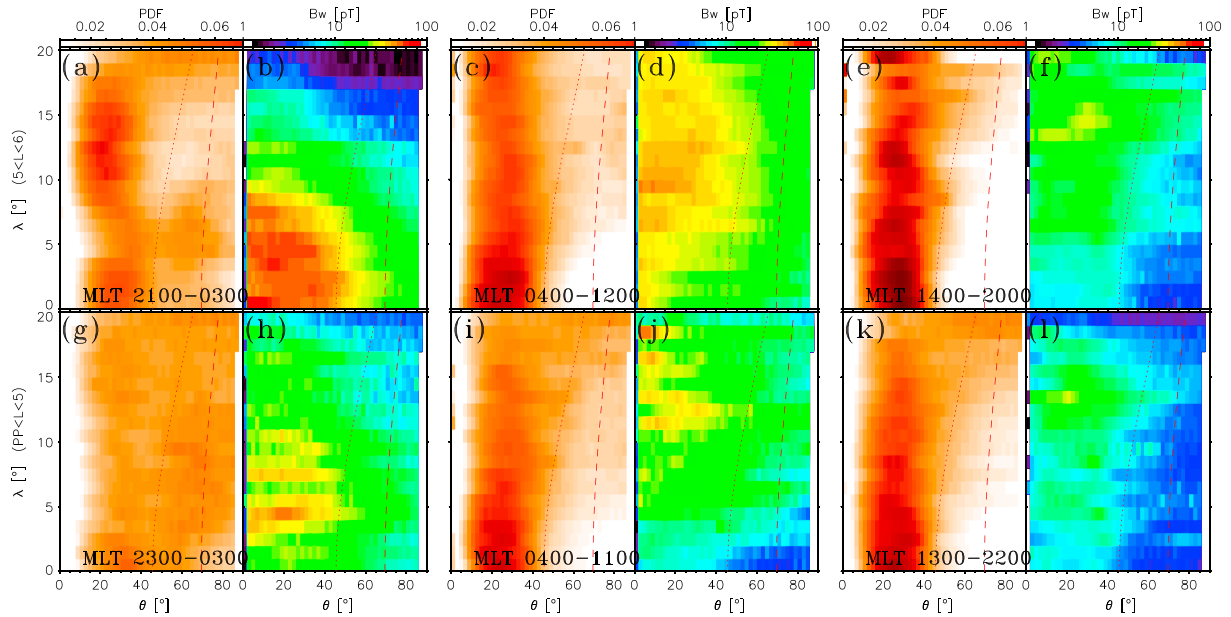| Sector	ij	0	1	2	3
		Night/Morning (MLT 23−04)			
PP < L < 5	1	$-1.6254\cdot10^{-1}$	$3.6771\cdot10^{-1}$	$5.8045\cdot10^{-2}$	$-1.1444\cdot10^{-2}$
	2	$6.2632\cdot10^{-1}$	1.6057	$-7.6047\cdot10^{-001}$	$7.6240\cdot10^{-2}$
	3	$-6.5017\cdot10^{-1}$	-4.1088	1.5400	$-1.2853\cdot10^{-1}$
	4	$3.3386\cdot10^{-1}$	1.9030	$-7.0627\cdot10^{-1}$	$4.3511\cdot10^{-2}$
5 < L < 6	1	$-1.9243\cdot10^{-2}$	$8.7220\cdot10^{-1}$	$-1.8186\cdot10^{-001}$	$1.2765\cdot10^{-2}$
	2	$-3.1598\cdot10^{-1}$	1.5395	$-5.9937\cdot10^{-1}$	$6.0658\cdot10^{-2}$
	3	$3.2857\cdot10^{-1}$	-4.0161	1.3777	$-1.4011\cdot10^{-1}$
	4	$-8.1296\cdot10^{-2}$	1.5803	$-5.3373\cdot10^{-1}$	$5.5854\cdot10^{-2}$
		Day (MLT 04−12)			
PP < L < 5	1	$1.2518\cdot10^{-1}$	$-4.2436\cdot10^{-1}$	$3.9558\cdot10^{-1}$	$-5.8637\cdot10^{-2}$
	2	$1.9141\cdot10^{-1}$	3.2038	-1.5388	$2.1615\cdot10^{-1}$
	3	$-4.6139\cdot10^{-1}$	-4.1311	1.7750	$-2.5385\cdot10^{-1}$
	4	$1.7790\cdot10^{-1}$	1.5620	$-6.5042\cdot10^{-1}$	$9.5267\cdot10^{-2}$
5 < L < 6	1	$1.1724\cdot10^{-1}$	$-1.6817\cdot10^{-002}$	$2.0852\cdot10^{-1}$	$-3.2907\cdot10^{-2}$
	2	$-8.8099\cdot10^{-2}$	3.0843	-1.4429	$1.6693\cdot10^{-1}$
	3	$-2.3276\cdot10^{-2}$	-4.5053	1.8765	$-2.0416\cdot10^{-1}$
	4	$-1.7350\cdot10^{-2}$	1.6932	$-6.7955\cdot10^{-1}$	$7.1511\cdot10^{-002}$
		Evening (MLT 12−23)			
Evening PP < L < 5	1	$-1.9255\cdot10^{-1}$	$2.5527\cdot10^{-1}$	$-3.5588\cdot10^{-2}$	$2.9532\cdot10^{-3}$
	2	1.0998	-1.6752	$6.3629\cdot10^{-1}$	$-7.3056\cdot10^{-2}$
	3	-1.0636	1.9950	$-8.1513\cdot10^{-1}$	$9.7581\cdot10^{-2}$
	4	$2.7847\cdot10^{-1}$	$-6.2123\cdot10^{-1}$	$2.6997\cdot10^{-1}$	$-3.4095\cdot10^{-2}$
Evening 5 < L < 6	1	$-6.7241\cdot10^{-2}$	$-1.7630\cdot10^{-1}$	$1.7162\cdot10^{-1}$	$-2.3834\cdot10^{-2}$
	2	-1.0697	2.4856	-1.0111	$1.0833\cdot10^{-1}$
	3	1.7268	-3.5630	1.3882	$-1.5065\cdot10^{-1}$
	4	$-6.3818\cdot10^{-1}$	1.2429	$-4.9241\cdot10^{-1}$	$5.5083\cdot10^{-2}$

of UB chorus wave RMS amplitudes is presented in Figure 8 in the (λ, Kp) domain. A model of a form similar to a previous model (Agapitov et al., 2015) is used to represent the dependence of UB chorus amplitude on λ and geomagnetic activity (Kp index here):

$$\lg(B_w(\lambda, Kp)[\text{nT}]) = \sum \sum a_{ij} Kp^j \lambda^i \qquad (2)$$

where the coefficients a_{ij} have been evaluated mainly based on Van Allen Probe measurements. The model is shown in Figure 8 by contour lines with colors corresponding to wave amplitude levels. The coefficients of the model are listed in Table 2.

4. Synthetic Model of Wave Normal Angle Distribution of Lower-Band Chorus Waves

The distribution $g(\theta)$ of chorus wave normal angles θ (the angle between their direction of propagation and the geomagnetic field lines) is also crucially important for calculating diffusion rates (Albert, 2017; Artemyev et al., 2013, 2015, 2016; Li et al., 2014; Mourenas et al., 2014; Shprits & Ni, 2009). This distribution $g(\theta)$ has been shown to depend on L, MLT, latitude, and geomagnetic activity (Agapitov et al., 2013, 2015; Artemyev et al., 2016). The presence of a subpopulation of highly oblique LB waves $\theta \in [\theta_g, \theta_r]$ has been recently revealed by Time History of Events and Macroscale Interactions during Substorms (THEMIS), Cluster, and Van Allen Probe studies (Agapitov et al., 2013, 2014, 2015; Artemyev et al., 2015; Li et al., 2011; Li, Santolik, et al., 2016) where θ_g and θ_r are, respectively, the Gendrin and resonance cone angles (Gendrin, 1961). The mean

Figure 9. Distributions of amplitudes and wave normal angles of lower-band chorus waves in the λ/θ domain in two L ranges for the same MLT ranges as in Figure 8, based on combined statistics from Cluster and the Van Allen Probes. The Gendrin and resonance cone angles calculated for $f = 0.35f_{ce}$ are indicated by the red dotted and dashed curves, respectively. The resonance cutoff is calculated for $f = 0.1f_{ce}$.

magnetic wave power of such highly oblique waves is generally smaller than for parallel waves (Santolík et al., 2014; Li, Santolik, et al., 2016), but their effect on electrons can become important during quiet to moderately disturbed periods (Artemyev et al., 2013, 2015; Li et al., 2014; Mourenas et al., 2014).
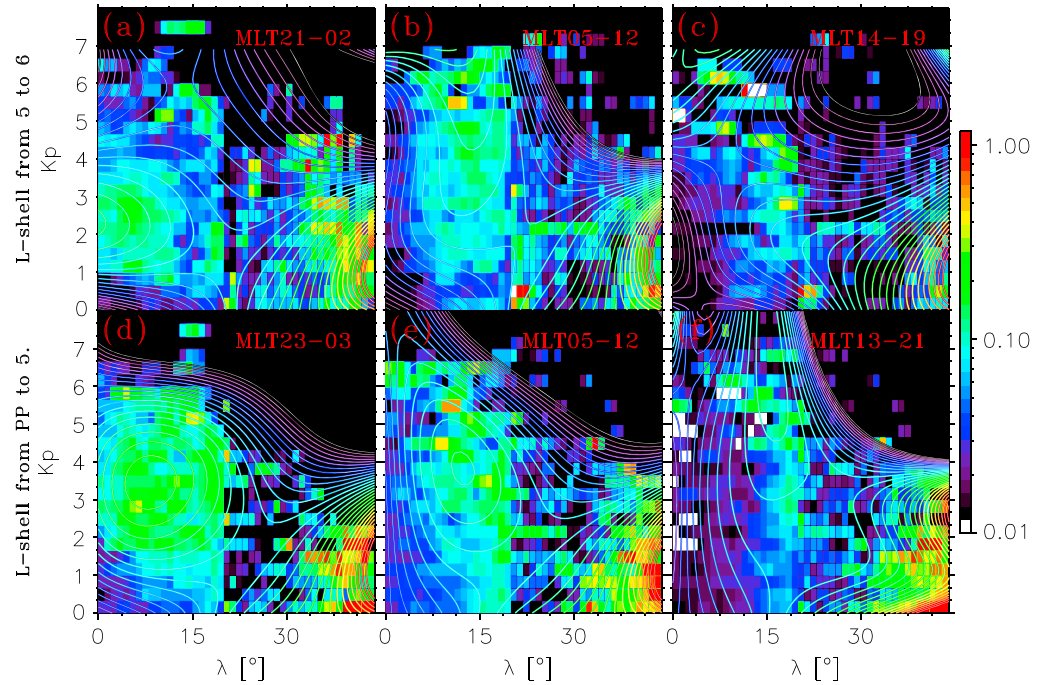
The presence of such very oblique LB chorus waves at low latitudes may be explained by different generation mechanisms involving temperature anisotropy at high energy (keVs) and reduced Landau damping at lower energy. The very oblique versus parallel wave intensity distributions have also been discussed and tentatively explained based on nonlinear effects (Agapitov et al., 2016; Artemyev et al., 2016; Gao et al., 2016; Li, Mourenas, et al., 2016; Mourenas, Artemyev, Agapitov, Krasnoselskikh, Mozer, 2015). At higher latitudes, there is a competition between the increase (and spreading) of wave normal angles during wave propagation toward higher latitudes in the inhomogeneous geomagnetic field (e.g., Breuillard et al., 2012) and Landau damping of the most oblique whistler-mode waves (Chen et al., 2013). This competition likely explains the different $g(\theta)$ distributions with latitude and geomagnetic activity observed in different spatial sectors (Artemyev et al., 2016).

The distributions of LB chorus wave occurrences and amplitudes as a function of λ and θ are presented in Figure 9 for the same MLT sectors as in Figure 1. A significant population of highly oblique waves is observed in the night sector, starting from the equator. While magnetic amplitudes of the very oblique waves are lower than for quasi-parallel waves, the electric field component of this population can be exceptionally large (up to 200 mV/m) and may lead to efficient nonlinear interactions through trapping via Landau resonance (Agapitov et al., 2015, 2016). In the morning sector, day sector, and especially in the evening sector, the population of very oblique LB chorus is negligible around the equator. Some very oblique LB waves start to be observed above $\sim15°$, presumably due to propagation effects (see details in Agapitov et al., 2013).

The integral characteristics of the LB chorus distribution of θ can be represented (similar as in Agapitov et al., 2015) under the form of a sum of two Gaussians with parameters θ_1, θ_2, $\delta\theta_1$, and $\delta\theta_2$ only weakly dependent on λ: (Artemyev et al., 2013; Mourenas et al., 2014):

$$g(\theta) = \exp\left(-\frac{(\theta - \theta_1)^2}{\delta\theta_1^2}\right) + Q^2 \exp\left(-\frac{(\theta - \theta_2)^2}{\delta\theta_2^2}\right) \tag{3}$$

where the factor Q depends on Kp, L shell, as well as on geomagnetic latitude and MLT. Parameters θ_1, θ_2, $\delta\theta_1 \approx \delta\theta_2$ have already been determined by Agapitov et al. (2015) and can be approximated by polynomials

Figure 10. Distribution of obliquity factor Q describing the amount of very oblique LB chorus waves based on Van Allen Probes ($\lambda < 20°$) and Cluster ($\lambda > 20°$) measurements, shown by solid colors for three MLT (indicated in the panels) sectors and two L shell ranges. The synthetic models of Q as a continuous function of Kp and λ are shown by contours of corresponding color in the day, evening, and night sectors of the magnetosphere for $L \sim 4$–5 and $L = 5$–6 above the plasmapause.

as a function of latitude ($\delta\theta_1 \approx \delta\theta_2 \approx 8°$): $\theta_1 = 11.5 + 14.3\lambda - 8.1\lambda^2 + 1.2\lambda^3$, and $\theta_2 = 66 + 0.1\lambda$. The factor Q is shown in Figure 10, demonstrating a dependence on Kp known already from Cluster data (Agapitov et al., 2015): the wave normal angle distribution evolves from quasi-parallel during very quiet times ($Kp < 1$) to more oblique for intermediate geomagnetic activity $Kp = 1$–5, until the presence of very oblique waves drops again when $Kp > 5$–6. Similar as in Agapitov et al. (2015), the synthetic model for Q is calculated in a form

$$Q(\lambda, Kp) = \sum_{i=0}^{i=4} b_{ij}\lambda^i Kp^j \qquad (4)$$

where $0 \leq Kp < 7$. The corresponding coefficients are provided in Table 3. The result model distribution of Q is shown in Figure 10 by contour lines.

The overall orbital coverage of the considered satellites still imposes some limits for the applicability of the present model. In the domain with large $Kp > 7$ or at latitudes $> 35°$, Cluster coverage is very sparse. To take this into account, we have multiplied the model Q by a Heaviside function $H((7 - Kp) \cdot (35° - \lambda))$ where $H(x) = 0$ if $x < 0$, $H = 1$ if $x > 0$. Finally, to get a realistic model of Q, one must also take into account that $Q < 0.07$ involves rare observations of very oblique waves. At low latitudes $\lambda < 10°$, previous Van Allen Probe studies (Agapitov et al., 2016; Li, Santolik, et al., 2016) suggest that very oblique waves are more likely to be observed during periods without parallel waves, so that a small time averaged Q actually corresponds to very rare occurrences of highly oblique waves with finite RMS amplitudes. Since our statistical wave model aims at providing the typical waves encountered by electrons over limited periods (days), and since moderate amplitude, very oblique waves are mainly effective for electron scattering when they are observed regularly (Artemyev et al., 2016), such rare occurrences should better be set to zero in the average Q model. The final expression of the average wave obliqueness Q_{av} is therefore $Q_{av} = Q \cdot H(0.07 - Q)$ with H the Heaviside function.

UB chorus waves are known to be more oblique in general than LB chorus waves (Meredith et al., 2012), with wave normal angles increasing with latitude. Such properties can also be seen in the distributions presented in Figure 11. However, their localization in a relatively narrow latitude range ($|\lambda| < 7°$) allows to simplify the

Table 3
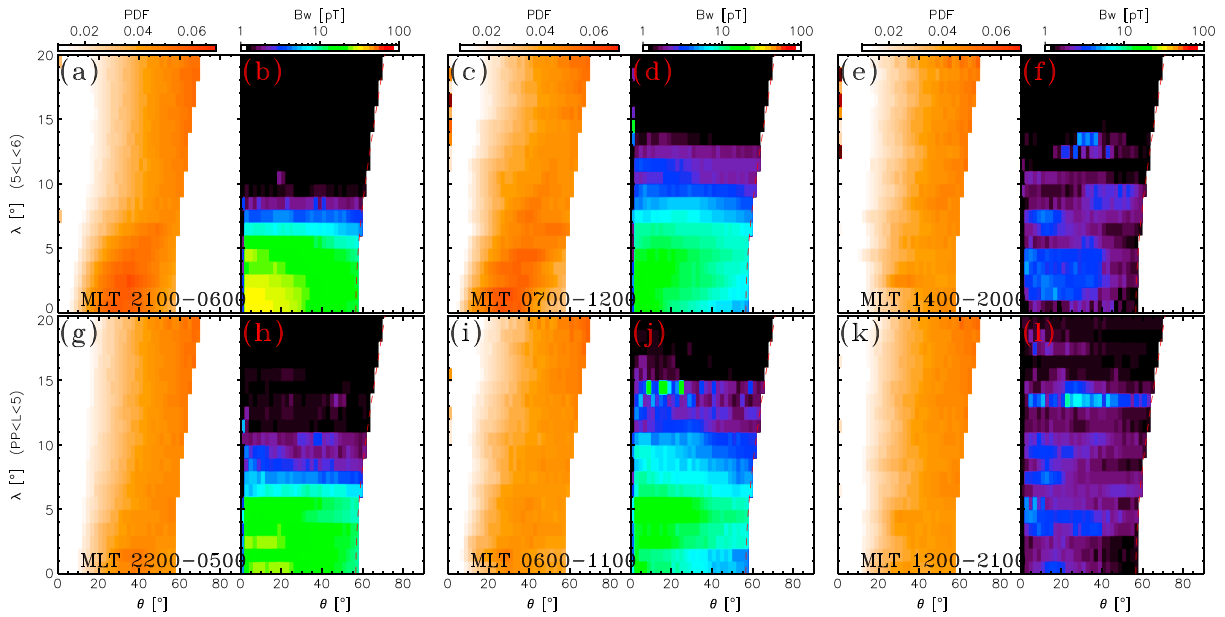*Coefficients α_{ij} for the Model of LB Chorus Wave Obliqueness Q*

Sector	ij	0	1	2	3
		Night/Morning (MLT 23–04)			
$PP < L < 5$	1	-1.7349	$4.3573 \cdot 10^{-1}$	$-5.8471 \cdot 10^{-2}$	$-1.0832 \cdot 10^{-3}$
	2	$3.1458 \cdot 10^{-1}$	$4.7479 \cdot 10^{-2}$	$4.2994 \cdot 10^{-2}$	$-9.9595 \cdot 10^{-3}$
	3	$-2.7001 \cdot 10^{-2}$	$-2.9056 \cdot 10^{-1}$	$4.9767 \cdot 10^{-2}$	$-9.4552 \cdot 10^{-5}$
	4	$6.7197 \cdot 10^{-3}$	$6.7163 \cdot 10^{-2}$	$-1.6999 \cdot 10^{-2}$	$7.8397 \cdot 10^{-4}$
$5 < L < 6$	1	-2.0375	1.1006	$-3.2083 \cdot 10^{-1}$	$2.3609 \cdot 10^{-2}$
	2	$3.8130 \cdot 10^{-1}$	$-4.3414 \cdot 10^{-1}$	$9.6520 \cdot 10^{-2}$	$-2.4317 \cdot 10^{-3}$
	3	$-5.9988 \cdot 10^{-3}$	$-1.4423 \cdot 10^{-1}$	$6.8570 \cdot 10^{-2}$	$-9.0388 \cdot 10^{-3}$
	4	$2.3391 \cdot 10^{-3}$	$5.2339 \cdot 10^{-2}$	$-2.2772 \cdot 10^{-2}$	$2.5075 \cdot 10^{-3}$
		Day (MLT 04–12)			
$PP < L < 5$	1	-1.5602	$-1.7421 \cdot 10^{-2}$	$7.8850 \cdot 10^{-3}$	$-3.5903 \cdot 10^{-4}$
	2	$2.8115 \cdot 10^{-1}$	$3.8588 \cdot 10^{-1}$	$-5.7127 \cdot 10^{-2}$	$1.2217 \cdot 10^{-3}$
	3	$-4.0365 \cdot 10^{-2}$	$-3.7408 \cdot 10^{-1}$	$9.6688 \cdot 10^{-2}$	$-8.5532 \cdot 10^{-3}$
	4	$9.6760 \cdot 10^{-3}$	$7.4221 \cdot 10^{-2}$	$-2.4127 \cdot 10^{-2}$	$2.3367 \cdot 10^{-3}$
$5 < L < 6$	1	-1.5602	$-1.7421 \cdot 10^{-2}$	$7.8850 \cdot 10^{-3}$	$-3.5903 \cdot 10^{-4}$
	2	$2.8115 \cdot 10^{-1}$	$3.8588 \cdot 10^{-1}$	$-5.7127 \cdot 10^{-2}$	$1.2217 \cdot 10^{-3}$
	3	$-4.0365 \cdot 10^{-2}$	$-3.7408 \cdot 10^{-1}$	$9.6688 \cdot 10^{-2}$	$-8.5532 \cdot 10^{-3}$
	4	$9.6760 \cdot 10^{-3}$	$7.4221 \cdot 10^{-2}$	$-2.4127 \cdot 10^{-2}$	$2.3367 \cdot 10^{-3}$
		Evening (MLT 12–23)			
$PP < L < 5$	1	-1.6350	$-3.6730 \cdot 10^{-2}$	$-5.8389 \cdot 10^{-3}$	$2.6194 \cdot 10^{-3}$
	2	$4.0211 \cdot 10^{-1}$	$2.5088 \cdot 10^{-1}$	$2.2223 \cdot 10^{-2}$	$-1.4524 \cdot 10^{-2}$
	3	$-1.2924 \cdot 10^{-1}$	$-1.3873 \cdot 10^{-1}$	$-4.8244 \cdot 10^{-2}$	$1.7654 \cdot 10^{-2}$
	4	$3.3448 \cdot 10^{-2}$	$-7.0435 \cdot 10^{-3}$	$2.6980 \cdot 10^{-2}$	$-6.3613 \cdot 10^{-3}$
$5 < L < 6$	1	-1.6088	$-6.7795 \cdot 10^{-1}$	$2.6775 \cdot 10^{-1}$	$-2.3058 \cdot 10^{-2}$
	2	$-5.8653 \cdot 10^{-1}$	1.9588	$-6.9747 \cdot 10^{-1}$	$6.4197 \cdot 10^{-2}$
	3	$3.8417 \cdot 10^{-1}$	$-9.5007 \cdot 10^{-1}$	$3.2970 \cdot 10^{-1}$	$-3.1692 \cdot 10^{-2}$
	4	$-4.0524 \cdot 10^{-2}$	$1.2955 \cdot 10^{-1}$	$-4.6650 \cdot 10^{-2}$	$4.6566 \cdot 10^{-3}$

fit of the θ distribution under the form of a constant $\theta_m = 30°$ and variance $\delta\theta = 18°$, independent of λ, but with an upper cutoff imposed by the resonance cone angle.

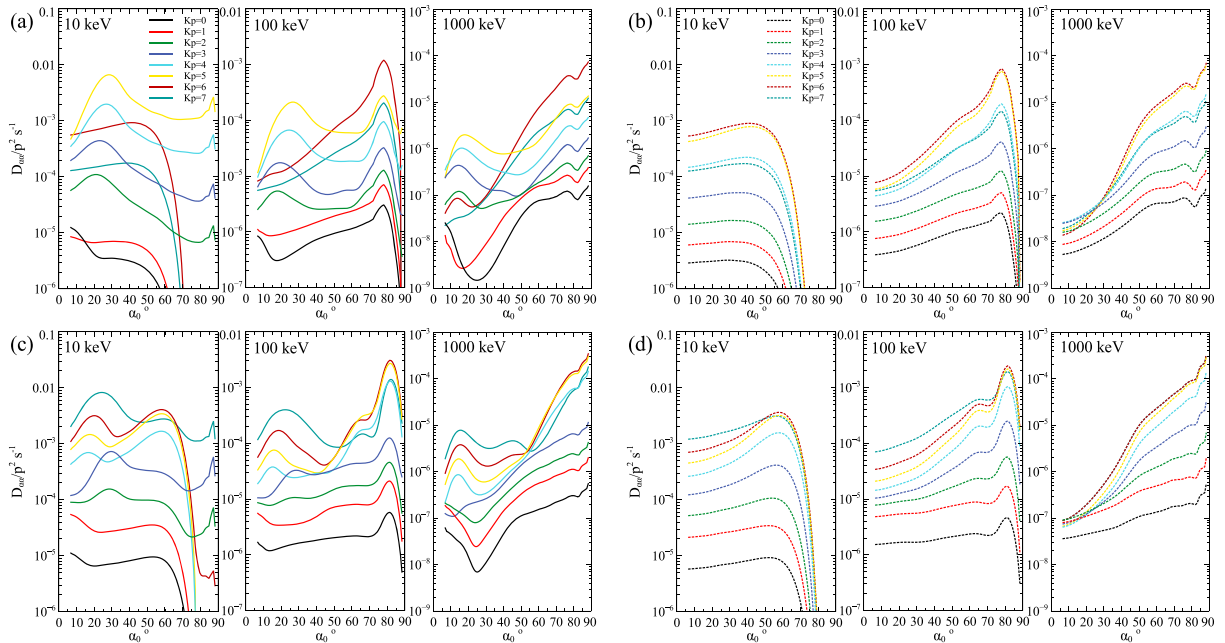## 5. Diffusion Rate Calculations Using the Synthetic Chorus Model

The importance of using the new, more realistic, synthetic chorus wave model presented here, as compared with a less comprehensive model (e.g., Agapitov et al., 2015), can be assessed by comparing the resulting diffusion rates of electrons. Accordingly, pitch angle diffusion rates have been numerically evaluated based on the new synthetic chorus model and then compared with diffusion rates calculated with a previous chorus model derived from Cluster data alone (Agapitov et al., 2015).

At $L \sim 4.5$, Figure 12 demonstrates that considering a realistic distribution of wave obliquity Q results in a significant increase of ~ 10 keV electron scattering for low pitch angle particles. This effect is most pronounced during low and moderate geomagnetic activity ($Kp \lesssim 5$). A similar enhancement of scattering rates just above the loss cone is provided by highly oblique waves for $100 - 1,000$ keV electrons, except that it now occurs only for $1 < Kp < 6$. At $L = 6$, the increase of pitch angle diffusion near the loss cone occurs when $1 < Kp < 6$ at all energies from 10 keV to 1 MeV. Such diffusion enhancements are expected to reduce the lifetimes of electrons (Artemyev et al., 2013, 2016; Mourenas et al., 2014, 2013). Note that the wave refractive index N of oblique whistler mode waves is likely limited by hot plasma effects near the resonance cone, requiring to use an upper limit $N < 300$ at most for diffusion rate calculations (Artemyev et al., 2016; Li et al., 2014; Mourenas et al., 2014).
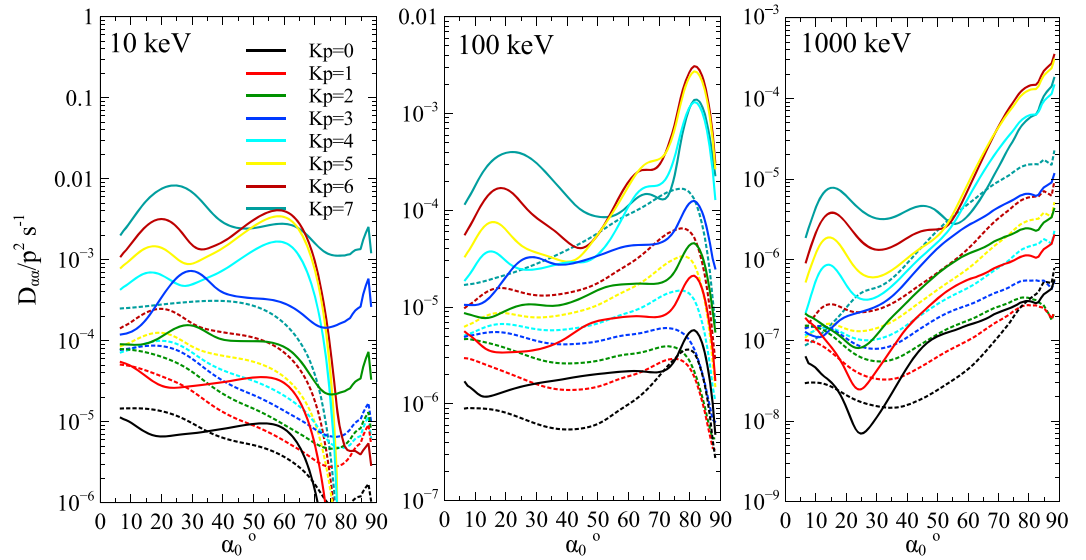
Figure 11. Distributions of amplitudes and wave normal angle θ of UB chorus waves in the λ/θ domain over two L ranges for the same MLT ranges as in Figure 1c, based on combined wave statistics from Cluster and the Van Allen Probes.

Figure 13 shows that MLT-averaged pitch angle scattering rates at $L = 6$ are strongly enhanced for nearly equatorial (i.e., high equatorial pitch angle) 10–1,000 eV electrons when $Kp > 2$ as compared with results based on a previous chorus model solely based on Cluster data (Agapitov et al., 2015) with a much smaller increase near the loss cone. This mainly stems from the high chorus wave intensity observed at magnetic latitudes $\leq 20°$ in Van Allen Probe statistics, in a domain where Cluster orbital coverage was insufficient for a precise description of the wave intensity distribution.

Figure 12. MLT-averaged pitch angle diffusion rates for three electron energies and (a) $L = 4.5$ with the Q model given by equation (4), (b) $L = 4.5$ and $Q = 0$, (c) $L = 6.0$ with the Q model given by equation (4), and (d) $L = 6.0$ and $Q = 0$. Equatorial plasma density is given by the model from Sheeley et al. (2001), whereas the plasma density variation with λ is provided by the model from Denton et al. (2006). Resonant roots are calculated for ± 50 cyclotron harmonics. The full cold plasma dispersion is used (Stix, 1962) with a maximum value of the wave refractive index N defined by hot plasma effects near the resonance cone ($N < 300$, see details in Mourenas et al., 2014).
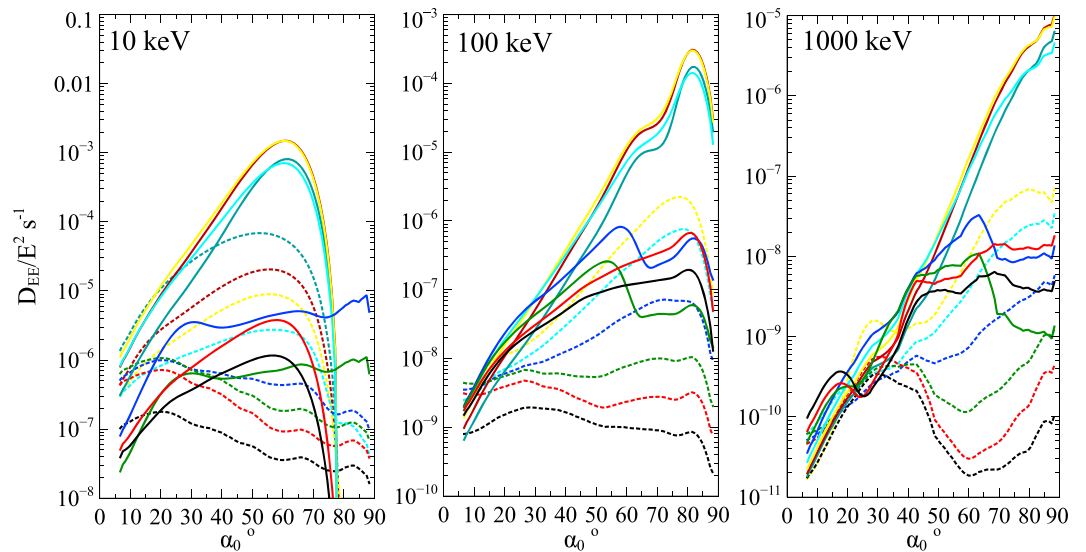
Figure 13. Comparison of MLT-averaged pitch angle diffusion rates evaluated at $L = 6$ using the new synthetic chorus model (solid curve) or the previous Cluster-only model of chorus waves from Agapitov et al. (2015) (dotted curves).

Finally, Figure 14 shows energy diffusion rates calculated at $L = 5.5$ near midnight MLT using the new synthetic chorus model, compared with energy diffusion rates obtained using a previous Cluster-only chorus model (Agapitov et al., 2015). One finds a very strong increase of energy diffusion due to the significantly higher wave intensity at low latitudes in the new model. Since most energy diffusion of relativistic electrons generally occurs on the nightside (Mourenas et al., 2014; Thorne et al., 2013), one expects a considerable enhancement of relativistic electron fluxes produced by chorus-induced energization during disturbed periods when using the new synthetic chorus model as compared with the earlier model.

6. Discussion and Conclusions

In this paper, we have provided a new, synthetic model of chorus waves derived from a careful examination of combined statistics from the Van Allen Probes (at low latitudes) and Cluster satellites (at higher latitudes). This model includes different continuous fits for the wave amplitude, wave frequency, and wave normal angle

Figure 14. Energy diffusion rates calculated at $L = 5.5$ and midnight MLT for three different electron energies, using the new synthetic lower-band chorus model (solid curves) or the Cluster-only chorus model (Agapitov et al., 2015) (dotted curves).

as a function of Kp, magnetic latitude λ, and MLT, in two L sectors (<5 and $\sim 5-6$) above the plasmapause. The poor orbital coverage at high latitudes by the Van Allen Probes is compensated by the good coverage from Cluster, while the low Cluster coverage at low latitudes in the night sector and high L is compensated by the excellent coverage there by the Van Allen Probes. These two data sets have been cross calibrated in the overlap region $\lambda \sim 15° - 20°$. As a result, our final synthetic model provides the wave distribution from the equator up to $\lambda = 45°$ for $Kp = 0-6(7)$ and $L \sim 4-7$. The results of this comprehensive analysis have shown the following.

1. The lower-band chorus wave intensity given by equation (1) is strongly increased at low latitudes for $L = 5-6$ as compared with a previous model (Agapitov et al., 2015) derived solely from Cluster data (which was sparse in this domain). This should explain the much stronger electron energization up to MeVs in this crucial region of the outer radiation belt (Horne et al., 2005; Mourenas et al., 2014; Su et al., 2015; Thorne et al., 2013; Tu et al., 2014).

2. The wave normal angular distribution of LB chorus given by equations (3) and (4) is in general agreement with previous results from Agapitov et al. (2015). A relatively new point is the significant population of very oblique waves recorded in the night sector by the Van Allen Probes at low latitudes during disturbed periods ($Kp \sim 3-6$).

3. The wave frequency strongly depends on latitude (as reported earlier by Breuillard et al., 2012, 2015 and Bunch et al., 2013), which is explained by the L shell drift of the waves along their propagation inside the magnetosphere. An interesting issue concerns the different distributions of quasi-parallel and very oblique LB chorus waves: quasi-parallel waves have in general lower mean frequency but greater variance. Both these dependencies are roughly linear functions of λ with a mean frequency decreasing toward $\sim 0.2 f_{ce}$ as latitude increases (see formulas in section 2.2. This shifts the latitudinal location of resonances with electrons toward regions of higher LB chorus amplitudes and should therefore be taken into account in radiation belt codes.

4. UB chorus waves are located in the vicinity of the geomagnetic equator ($|\lambda| < 5-7°$) due to higher (compared to LB chorus) damping rates (Chen et al., 2013). Their wave power given by equation (2) is concentrated in the frequency range $f \sim (0.5-0.6) f_{ce}$ with a mean value of $0.55 f_{ce}$ and a variance of $0.05 f_{ce}$. The wave normal angle distribution of UB chorus is in general more oblique ($\theta_m \sim 30°$) than for LB chorus and does not vary significantly over the narrow λ range of UB chorus observations.

Further, using the proposed new synthetic model of lower-band chorus to calculate electron pitch angle and energy diffusion rates, we have shown that this more realistic and comprehensive wave model leads to strong variations in quasi-linear diffusion rates of $10-1000$ eV particles at $L = 4-6$ as compared, for example, with results obtained with the previous Cluster-only chorus model from Agapitov et al. (2015), thanks to the considerably improved data statistics provided by the Van Allen Probes at low magnetic latitudes. In particular, pitch angle and especially energy diffusion rates are strongly increased near the equator, whereas pitch angle diffusion near the loss cone is also enhanced due to both slightly increased wave amplitudes and a nonnegligible presence of highly oblique lower-band chorus waves. One expects significant impacts on modeling of relativistic electron energization and loss in the outer radiation belt, especially during disturbed periods ($Kp \sim 3-6$).

References

Agapitov, O., Artemyev, A., Krasnoselskikh, V., Khotyaintsev, Y. V., Mourenas, D., Breuillard, H., ... Rolland, G. (2013). Statistics of whistler mode waves in the outer radiation belt: Cluster STAFF-SA measurements. *Journal of Geophysical Research: Space Physics*, 118, 3407–3420. https://doi.org/10.1002/jgra.50312

Agapitov, O., Artemyev, A., Mourenas, D., Krasnoselskikh, V., Bonnell, J., Contel, O., ... Cully, C. M. (2014). The quasi-electrostatic mode of chorus waves and electron nonlinear acceleration. *Journal of Geophysical Research: Space Physics*, 119, 1606–1626. https://doi.org/10.1002/2013JA019223

Agapitov, O., Artemyev, A. V., Mourenas, D., Mozer, F. S., & Krasnoselskikh, V. (2015). Empirical model of lower band chorus wave distribution in the outer radiation belt. *Journal of Geophysical Research: Space Physics*, 120, 10,425–10,442. https://doi.org/10.1002/2015JA021829

Agapitov, O., Mourenas, D., Artemyev, A. V., & Mozer, F. S. (2016). Exclusion principle for very oblique and parallel lower band chorus waves. *Geophysical Research Letters*, 43, 11,112–11,120. https://doi.org/10.1002/2016GL071250

Albert, J. M. (2017). Quasi-linear diffusion coefficients for highly oblique whistler mode waves. *Journal of Geophysical Research: Space Physics*, 122, 5339–5354. https://doi.org/10.1002/2017JA024124

Albert, J. M. (2007). Simple approximations of quasi-linear diffusion coefficients. *Journal of Geophysical Research*, 112, A12202. https://doi.org/10.1029/2007JA012551

Albert, J. M. (2008). Efficient approximations of quasi-linear diffusion coefficients in the radiation belts. *Journal of Geophysical Research*, 113, A06208. https://doi.org/10.1029/2007JA012936

Artemyev, A., Agapitov, O., Mourenas, D., Krasnoselskikh, V., & Zelenyi, L. M. (2013). Storm-induced energization of radiation belt electrons: Effect of wave obliquity. *Geophysical Research Letters*, *40*, 4138–4143. https://doi.org/10.1002/grl.50837

Artemyev, A., Agapitov, O., Mourenas, D., Krasnoselskikh, V., & Mozer, F. S. (2015). Wave energy budget analysis in the Earth's radiation belts uncovers a missing energy. *Nature Communications*, *6*, 8143. https://doi.org/10.1038/ncomms8143

Artemyev, A., Agapitov, O., Mourenas, D., Krasnoselskikh, V., Shastun, V., & Mozer, F. (2016). Oblique whistler-mode waves in the Earth's inner magnetosphere: Energy distribution, origins, and role in radiation belt dynamics. *Space Science Reviews*, *200*, 261–355. https://doi.org/10.1007/s11214-016-0252-5

Breuillard, H., Zaliznyak, Y., Krasnoselskikh, V., Agapitov, O., Artemyev, A., & Rolland, G. (2012). Chorus wave-normal statistics in the Earth's radiation belts from ray tracing technique. *Annales de Geophysique*, *30*, 1223–1233. https://doi.org/10.5194/angeo-30-1223-2012

Breuillard, H., Agapitov, O., Artemyev, A., Kronberg, E. A., Haaland, S. E., Daly, P. W., . . . Rolland, G. (2015). Field-aligned chorus wave spectral power in Earth's outer radiation belt. *Annales Geophysicae*, *33*(5), 583–597. https://doi.org/10.5194/angeo-33-583-2015

Bunch, N. L., Spasojevic, M., Shprits, Y. Y., Gu, X., & Foust, F. (2013). The spectral extent of chorus in the off-equatorial magnetosphere. *Journal of Geophysical Research: Space Physics*, *118*, 1700–1705. https://doi.org/10.1029/2012JA018182

Burtis, W. J., & Helliwell, R. A. (1976). Magnetospheric chorus: Occurrence patterns and normalized frequency. *Planetary and Space Science*, *24*, 1007–1024. https://doi.org/10.1016/0032-0633(76)90119-7

Chen, L., Thorne, R. M., Li, W., & Bortnik, J. (2013). Modeling the wave normal distribution of chorus waves. *Journal of Geophysical Research: Space Physics*, *118*, 1074–1088. https://doi.org/10.1029/2012JA018343

Cornilleau-Wehrlin, N., Chanteur, G., Perraut, S., Rezeau, L., Robert, P., Roux, A., . . . Staff Team (2003). First results obtained by the Cluster STAFF experiment. *Annales Geophysicae*, *21*, 437–456. https://doi.org/10.5194/angeo-21-437-2003

Denton, R. E., Takahashi, K., Galkin, I. A., Nsumei, P. A., Huang, X., Reinisch, B. W., . . . Hughes, W. J. (2006). Distribution of density along magnetospheric field lines. *Journal of Geophysical Research*, *111*, A04213. https://doi.org/10.1029/2005JA011414

Gao, X., Mourenas, D., Li, W., Artemyev, A. V., Lu, Q., Tao, X., & Wang, S. (2016). Observational evidence of generation mechanisms for very oblique lower band chorus using THEMIS waveform data. *Journal of Geophysical Research: Space Physics*, *121*, 6732–6748. https://doi.org/10.1002/2016JA022915

Gendrin, R. (1961). Le guidage des whistlers par le champ magnetique. *Planetary and Space Science*, *5*, 274–278. https://doi.org/10.1016/0032-0633(61)90096-4

Horne, R. B., Thorne, R. M., Shprits, Y. Y., Meredith, N. P., Glauert, S. A., Smith, A. J., . . . Decreau, P. M. E. (2005). Wave acceleration of electrons in the Van Allen radiation belts. *Nature*, *437*, 227–230. https://doi.org/10.1038/nature03939

Horne, R. B., Horne, R. B., Thorne, R. M., Glauert, S. A., Albert, J. M., Meredith, N. P., & Anderson, R. R. (2005). Timescale for radiation belt electron acceleration by whistler mode chorus waves. *Journal of Geophysical Research*, *110*, A03225. https://doi.org/10.1029/2004JA010811

Horne, R. B., Glauert, S. A., Meredith, N. P., Boscher, D., Maget, V., Heynderickx, D., & Pitchford, D. (2013). Space weather impacts on satellites and forecasting the Earth's electron radiation belts with SPACECAST. *Space Weather*, *11*, 169–186. https://doi.org/10.1002/swe.20023

Kletzing, C. A., Kurth, W. S., Acuna, M., MacDowall, R. J., Torbert, R. B., Averkamp, T., . . . Tyler, J. (2013). The Electric and Magnetic Field Instrument Suite and Integrated Science (EMFISIS) on RBSP. *Space Science Reviews*, *179*, 127–181. https://doi.org/10.1007/s11214-013-9993-6

LeDocq, M. J., Gurnett, D. A., & Hospodarsky, G. B. (1998). Chorus source locations from VLF Poynting flux measurements with the Polar spacecraft. *Geophysical Research Letters*, *25*(21), 4063–4066. https://doi.org/10.1029/1998GL900071

Li, W., Thorne, R. M., Bortnik, J., Nishimura, Y., Angelopoulos, V., Chen, L., . . . Bonnell, J. W. (2010). Global distributions of suprathermal electrons observed on THEMIS and potential mechanisms for access into the plasmasphere. *Journal of Geophysical Research*, *115*, A00J10. https://doi.org/10.1029/2010JA015687

Li, W., Bortnik, J., Thorne, R. M., & Angelopoulos, V. (2011). Global distribution of wave amplitudes and wave normal angles of chorus waves using THEMIS wave observations. *Journal of Geophysical Research*, *116*, A12205. https://doi.org/10.1029/2011JA017035

Li, W., Bortnik, J., Thorne, R. M., Cully, C. M., Chen, L., Angelopoulos, V., . . . LeContel, O. (2013). Characteristics of the Poynting flux and wave normal vectors of whistler-mode waves observed on THEMIS. *Journal of Geophysical Research: Space Physics*, *118*, 1461–1471. https://doi.org/10.1002/jgra.50176

Li, W., Mourenas, D., Artemyev, A. V., Agapitov, O. V., Bortnik, J., Albert, J. M., . . . Hospodarsky, G. B. (2014). Evidence of stronger pitch angle scattering loss caused by oblique whistler-mode waves as compared with quasi-parallel waves. *Geophysical Research Letters*, *41*, 6063–6070. https://doi.org/10.1002/2014GL061260

Li, W., Santolik, O., Bortnik, J., Thorne, R. M., Kletzing, C. A., Kurth, W. S., & Hospodarsky, G. B. (2016). New chorus wave properties near the equator from Van Allen Probes wave observations. *Geophysical Research Letters*, *43*, 4725–4735. https://doi.org/10.1002/2016GL068780

Li, W., Mourenas, D., Artemyev, A. V., Bortnik, J., Thorne, R. M., Kletzing, C. A., . . . Spence, H. E. (2016). Unraveling the excitation mechanisms of highly oblique lower band chorus waves. *Geophysical Research Letters*, *43*, 8867–8875. https://doi.org/10.1002/2016GL070386

Ma, Q., Mourenas, D., Artemyev, A., Li, W., Thorne, R. M., & Bortnik, J. (2016). Strong enhancement of 10–100 keV electron fluxes by combined effects of chorus waves and time domain structures. *Geophysical Research Letters*, *43*, 4683–4690. https://doi.org/10.1002/2016GL069125

Mauk, B. H., Fox, N. J., Kanekal, S. G., Kessel, R. L., Sibeck, D. G., & Ukhorskiy, A. (2012). Science objectives and rationale for the Radiation Belt Storm Probes mission. *Space Science Reviews*, *179*(1–4), 3–27. https://doi.org/10.1007/s11214-012-9908-y

Meredith, N. P., Horne, R. B., & Anderson, R. R. (2001). Substorm dependence of chorus amplitudes: Implications for the acceleration of electrons to relativistic energies. *Journal of Geophysical Research*, *106*, 13,165–13,178. https://doi.org/10.1029/2000JA900156

Meredith, N. P., Horne, R. B., Thorne, R. M., & Anderson, R. R. (2009). Survey of upper band chorus and ECH waves: Implications for the diffuse aurora. *Journal of Geophysical Research*, *114*, A07218. https://doi.org/10.1029/2009JA014230

Meredith, N. P., Horne, R. B., Sicard-Piet, A., Boscher, D., Yearby, K. H., Li, W., & Thorne, R. M. (2012). Global model of lower band and upper band chorus from multiple satellite observations. *Journal of Geophysical Research*, *117*, A10225. https://doi.org/10.1029/2012JA017978

Mourenas, D., Artemyev, A. V., Agapitov, O. V., & Krasnoselskikh, V. (2014). Consequences of geomagnetic activity on energization and loss of radiation belt electrons by oblique chorus waves. *Journal of Geophysical Research: Space Physics*, *119*, 2775–2796. https://doi.org/10.1002/2013JA019674

Mourenas, D., Artemyev, A. V., Agapitov, O. V., Krasnoselskikh, V., & Li, W. (2015). Approximate analytical solutions for the trapped electron distribution due to quasi-linear diffusion by whistler mode waves. *Journal of Geophysical Research: Space Physics*, *119*, 9962–9977. https://doi.org/10.1002/2014JA020443

Mourenas, D., Artemyev, A. V., Agapitov, O. V., Krasnoselskikh, V., & Mozer, F. S. (2015). Very oblique whistler generation by low-energy electron streams. *Journal of Geophysical Research: Space Physics*, *120*, 3665–3683. https://doi.org/10.1002/2015JA021135

Mourenas, D., Artemyev, A. V., Ma, Q., Agapitov, O. V., & Li, W. (2016). Fast dropouts of multi-MeV electrons due to combined effects of EMIC and whistler mode waves. *Geophysical Research Letters*, *43*, 4155–4163. https://doi.org/10.1002/2016GL068921

Ni, B., Thorne, R. M., Meredith, N. P., Shprits, Y. Y., & Horne, R. B. (2011). Diffuse auroral scattering by whistler mode chorus waves: Dependence on wave normal angle distribution. *Journal of Geophysical Research*, *116*, A10207. https://doi.org/10.1029/2011JA016517

Ni, B., Thorne, R. M., Meredith, N. P., Ma, Q., & Chen, L. (2013). Resonant scattering and resultant pitch angle evolution of relativistic electrons by plasmaspheric hiss. *Journal of Geophysical Research: Space Physics*, *118*, A10207. https://doi.org/10.1002/2013JA019260

Santolik, O., Gurnett, D. A., Pickett, J. S., Parrot, M., & Cornilleau-Wehrlin, N. (2004). A microscopic and nanoscopic view of storm-time chorus on 31 March 2001. *Geophysical Research Letters*, *31*, L02801. https://doi.org/10.1029/2003GL018757

Santolík, O., Macúsová, E., Kolmasová, I., Cornilleau-Wehrlin, N., & Conchy, Y. (2014). Propagation of lower-band whistler-mode waves in the outer Van Allen belt: Systematic analysis of 11 years of multi-component data from the Cluster spacecraft. *Geophysical Research Letters*, *41*, 2729–2737. https://doi.org/10.1002/2014GL059815

Sazhin, S. S., & Hayakawa, M. (1992). Magnetospheric chorus emissions—A review. *Planetary and Space Science*, *40*, 681–697. https://doi.org/10.1016/0032-0633(92)90009-D

Sheeley, B. W., Moldwin, M. B., Rassoul, H. K., & Anderson, R. R. (2001). An empirical plasmasphere and trough density model: CRRES observations. *Journal of Geophysical Research*, *106*, 25,631–25,642. https://doi.org/10.1029/2000JA000286

Shprits, Y. Y., & Ni, B. (2009). Dependence of the quasi-linear scattering rates on the wave normal distribution of chorus waves. *Journal of Geophysical Research*, *114*, A11205. https://doi.org/10.1029/2009JA014223

Shprits, Y. Y., Thorne, R. M., Horne, R. B., & Summers, D. (2006). Bounce-averaged diffusion coefficients for field-aligned chorus waves. *Journal of Geophysical Research*, *111*, A10225. https://doi.org/10.1029/2006JA011725

Shprits, Y. Y., Subbotin, D. A., Meredith, N. P., & Elkington, S. R. (2008). Review of modeling of losses and sources of relativistic electrons in the outer radiation belt II: Local acceleration and loss. *Journal of Atmospheric and Solar-Terrestrial Physics*, *70*, 1694–1713. https://doi.org/10.1016/j.jastp.2008.06.014

Spasojevic, M., & Shprits, Y. Y. (2013). Chorus functional dependencies derived from CRRES data. *Geophysical Research Letters*, *40*, 3793–3797. https://doi.org/10.1002/grl.50755

Stix, T. H. (1962). *The theory of plasma waves*. New York: McGraw-Hill.

Su, Z., Zhu, H., Xiao, F., Zheng, H., Wang, Y., Zong, Q.-G., . . . Baker, D. N. (2015). Quantifying the relative contributions of substorm injections and chorus waves to the rapid outward extension of electron radiation belt. *Journal of Geophysical Research: Space Physics*, *119*, 10,023–10,040. https://doi.org/10.1002/2014JA020709

Taubenschuss, U., Khotyaintsev, Y. V., Santolik, O., Vaivads, A., Cully, C. M., Le Contel, O., & Angelopoulos, V. (2014). Wave normal angles of whistler mode chorus rising and falling tones. *Journal of Geophysical Research: Space Physics*, *119*, 9567–9578. https://doi.org/10.1002/2014JA020575

Thorne, R. M., Thorne, R. M., Li, W., Ni, B., Ma, Q., Bortnik, J., . . . Kanekal, S. G. (2013). Rapid local acceleration of relativistic radiation-belt electrons by magnetospheric chorus. *Nature*, *504*, 411–414. https://doi.org/10.1038/nature12889

Tsurutani, B. T., & Smith, E. J. (1974). Postmidnight chorus: A substorm phenomenon. *Journal of Geophysical Research*, *79*, 118–127. https://doi.org/10.1029/JA079i001p00118

Tu, W., Cunningham, G. S., Chen, Y., Henderson, M. G., Camporeale, E., & Reeves, G. D. (2014). Modeling radiation belt electron dynamics during GEM challenge intervals with the DREAM3D diffusion model. *Journal of Geophysical Research: Space Physics,118*, 6197–6211. https://doi.org/10.1002/jgra.50560

Wygant, J. R., Bonnell, J. W., Goetz, K., Ergun, R. E., Mozer, F. S., Bale, S. D., . . . Tao, J. B. (2013). The Electric Field, and Waves (EFW) instruments on the Radiation Belt Storm Probes mission, *179*(1–4), 1830–220. https://doi.org/10.1007/s11214-013-0013-7